PHYSICAL REVIEW E **85**, 016308 (2012)

Two-fluid confined flow in a cylinder driven by a rotating end wall

P. T. Brady and M. Herrmann
School for Engineering of Matter, Transport and Energy, Arizona State University, Tempe, Arizona 85287, USA

J. M. Lopez
School of Mathematical and Statistical Sciences, Arizona State University, Tempe, Arizona 85287, USA and
Department of Mathematics, Kyungpook National University, Daegu, 702-701, South Korea

(Received 14 August 2011; revised manuscript received 7 December 2011; published 12 January 2012)

The flow of two immiscible fluids completely filling an enclosed cylinder and driven by the rotation of the bottom end wall is studied numerically. The simulations are in parameter regimes where there is significant advection of angular momentum, i.e., the disk rotation rate is fast compared to the viscous diffusion time. We consider two classes of scenarios. The first consists of cases that are straightforward to reproduce in physical experiments where only the rotation rate and the viscosity ratio of the fluids are varied. Then we isolate different forces acting on the system such as inertia, surface tension, and gravity by studying variations in individual governing parameters. The viscosity ratio determines how quickly the upper fluid equilibriates dynamically to the flow in the lower fluid and plays a major role in determining how vortex lines are bent in the neighborhood of the interface between the two fluids. This in turn determines the structure of the interfacial layer between the two swirling fluids, which is responsible for the flow in the upper fluid. The simulations show that even when there is significant interfacial deformation, both the dynamics and the equilibrium flow are dominated by vortex bending rather than vortex stretching. The simulations show that for the range of immiscible fluids considered, surface tension effects are significant. Increased surface tension reduces the degree to which the interface is deformed and the limit of zero surface tension is not an appropriate approximation.

DOI: 10.1103/PhysRevE.85.016308 PACS number(s): 47.55.−t, 47.15.−x

I. INTRODUCTION

There has been much interest in the flow in a cylinder driven by the rotation of the bottom when the top is a free surface [1–20]. Experimentally, the free surface is the interface between a liquid (typically water) and air. Some experiments [2,4,6,7,15] were conducted in regimes where the free surface remains essentially flat; however, other experiments [1,11,12, 14,18,19,21] have explored regimes where the deformation is of the order of the depth of the fluid layer. In modeling this problem, the flow on the air side of the interface has typically been ignored and for the most part the interface has been treated as flat and stress-free.

Very recent numerical simulations have allowed for small interface deformations [17], but they continued to assume the interface to be stress-free and ignored surface tension effects. In contrast, some experimental studies have considered the stress on the interface due to the presence of surface-active agents, which not only alter the surface tension but also impart surface viscosity to the interface [22–29]. In these swirling flows, the surface shear viscosity directly determines the angle at which vortex lines meet the interface. At a flat interface, the vortex lines are normal to the interface in the limit of zero surface shear viscosity and become tangential to the interface in the limit of very large surface shear viscosity, affecting the extent to which the interfacial flow rotates. The bending of the vortex lines very near the interface in order to accommodate the constraints imposed by the surface shear viscosity results in a thin and intense interfacial boundary layer whose azimuthal vorticity is comparable to that found if the interface were a stationary rigid lid [30].

Gas and liquid (in particular air and water) flows in the turbulent regime have also attracted much interest from geophysical applications [31] and industrial applications [32]. However, both theoretical modeling and numerical simulations have so far been restricted to the idealized situation where the interface is treated as being flat.

The characteristics of the interface between two immiscible (or weakly miscible) fluids have also attracted much attention, even when the density and viscosity differences are not as great as between air and water in the studies mentioned above. Such flows have been used extensively in laboratory experiments in order to model processes of the atmosphere and oceans [33–38]. Much of the theory for two-layer immiscible flows has focused on linear spin up or spin down, i.e., the transition from a state of solid-body rotation to another state of solid-body rotation when the change in rotation rate is very small compared to the mean rotation. The role of the boundary layers that form either side of the interface is a main concern for these studies [39–43]. More recently, these two-layer problems have been simulated numerically, relaxing some of the approximations made to allow for analytical progress [44], but still considering only spin up and spin down (albeit nonlinear) and neglecting surface tension effects.

Experimental observations in the strongly nonlinear regime have reported drastic changes in the topology of the interface as the shear increases [45]. The interfacial flow is strongly influenced by centrifugal acceleration and the interfacial flow alters the ambient flows. This two-way interaction appears stronger for small density differences and large viscosity differences between the two fluids [46]. What is still lacking is a nonlinear numerical investigation of two immiscible fluids with strong sustained shear across the interface.

In this paper we present such a numerical investigation allowing for large interface deformations and surface tension forces at the interface between the two fluids that are fully two-way coupled. We study the case where the bottom end wall is impulsively accelerated from rest to a constant rotation rate, accelerating the initially at rest fluids until they reach a steady state.

After presenting the governing equations and numerical methods in Sec. II, we discuss the effects of increasing the disk rotation rate (Sec. III A), analyze the impact of changing the viscosity ratio between the two fluids (Sec. III B), and explore the effects of inertia (Sec. III C), surface tension (Sec. III D), and gravity (Sec. III E).

II. GOVERNING EQUATIONS

Consider a cylinder of radius R and height H filled with two immiscible fluids with an initial interface height of h when everything is at rest. At $t = 0$, the bottom end wall is impulsively set to rotate with angular frequency Ω. The gravitational acceleration g is aligned with the axis of the cylinder. The density and viscosity of the bottom fluid are denoted by ρ_b and μ_b, respectively. Quantities with a b or t subscript denote the bottom or top fluid, respectively. The two fluids are characterized by their viscosity ratio $\mu_r = \mu_t/\mu_b$, density ratio $\rho_r = \rho_t/\rho_b$, and the interfacial tension between the fluids σ. Using R as the length scale and $1/\Omega$ as the time scale, the Navier-Stokes equations governing the motion of this unsteady, incompressible, two-fluid system are

$$\begin{aligned} &\rho\left(\frac{\partial \mathbf{u}}{\partial t} + \mathbf{u}\cdot\nabla\mathbf{u}\right) \\ &\quad = -\nabla P + \frac{1}{\mathrm{Re}}\nabla\cdot[\mu(\nabla\mathbf{u} + \nabla^T\mathbf{u})] + \frac{1}{\mathrm{We}}\kappa\delta\hat{\mathbf{n}} - \frac{1}{\mathrm{Fr}}\hat{\mathbf{z}}, \\ &\nabla\cdot\mathbf{u} = 0, \end{aligned} \tag{1}$$

where $\mathbf{u} = (u,v,w)$ is the velocity in cylindrical polar coordinates (r,θ,z), P is the pressure divided by the bottom fluid density ρ_b, κ is the interface curvature, δ is the interface delta function (nonzero only at the location of the interface), $\hat{\mathbf{n}}$ is the interface normal, and $\hat{\mathbf{z}}$ is the unit vector in the axial direction. The relative density $\rho = 1$ in the bottom fluid and $\rho = \rho_r$ in the top fluid and the relative dynamic viscosity $\mu = 1$ in the bottom fluid and $\mu = \mu_r$ in the top fluid. The Reynolds, Froude, and Weber numbers are given by

$$\mathrm{Re} = \frac{\rho_b R^2 \Omega}{\mu_b}, \quad \mathrm{Fr} = \frac{\Omega^2 R^2}{gh}, \quad \mathrm{We} = \frac{\rho_b R^3 \Omega^2}{\sigma}. \tag{2}$$

The problem is governed by the nondimensional parameters Re, We, and Fr; the material property ratios $\rho_r = \rho_t/\rho_b$ and $\mu_r = \mu_t/\mu_b$; the relative initial interface height h/R; and the cylinder aspect ratio H/R.

Of the many governing parameters in this problem, the geometric parameters h/R and H/R are the least interesting. This is because what is of interest in this class of problems is how the interface deforms in response to the governing parameters and in how the top fluid is driven into motion via the coupling across the interface as the bottom fluid is driven into motion. So long as the deformation of the interface does not bring the interfacial shear layer near either the top or bottom boundary layer, the two geometric parameters play only a secondary role. In the single-fluid version of this swirling flow problem, which has been studied extensively both experimentally and numerically (numerous papers are cited in the introduction), it is well established that the aspect ratio, so long as it is not too large or too small, has only a quantitative impact on the flow. Hence, we focus on variations of the governing parameters that are of primary importance.

A. Numerics

To determine the location $\mathbf{x}_f$ of the phase interface we employ a level-set approach by defining the level-set scalar at the interface

$$G(\mathbf{x}_f,t) = 0, \tag{3}$$

with $G(\mathbf{x},t) > 0$ in the bottom fluid and $G(\mathbf{x},t) < 0$ in the top fluid layer. Differentiating Eq. (3) with respect to time yields the level-set equation

$$\frac{\partial G}{\partial t} + \mathbf{u}\cdot\nabla G = 0. \tag{4}$$

The interface curvature κ can be expressed in terms of the level-set scalar as

$$\kappa = -\nabla\cdot\frac{\nabla G}{|\nabla G|}. \tag{5}$$

We solve and evaluate all level-set-related equations following the refined level-set grid method in a separate globally conservative level-set solver [47] using an auxiliary high-resolution G grid with a fifth-order weighted essentially nonoscillatory scheme [48] in conjunction with a third-order total-variation-diminishing Runge-Kutta time discretization [49]. Neumann boundary conditions for G on the cylinder side wall impose a 90° contact angle there. The phase interface curvature κ is evaluated on the G grid using a second-order-accurate interface projection method [47].

The balanced force algorithm for finite-volume solvers [47] is used to solve Eq. (1). The algorithm has been implemented in the flow solver NGA [50], which solves the Navier-Stokes equations using a second-order-accurate fractional step method on a staggered grid layout. The location of the phase interface essentially impacts directly three different terms in these equations. The first two, ρ and μ, can be calculated for finite-volume solvers by

$$\rho = \alpha_{\mathrm{CV}} + (1-\alpha_{\mathrm{CV}})\rho_r, \tag{6}$$

$$\mu = \alpha_{\mathrm{CV}} + (1-\alpha_{\mathrm{CV}})\mu_r, \tag{7}$$

where α_{CV} is the bottom fluid phase volume fraction of a control volume,

$$\alpha_{\mathrm{CV}} = 1/V_{\mathrm{CV}}\int_{V_{\mathrm{CV}}}\mathcal{H}(G)dV, \tag{8}$$

with V_{CV} the volume of the control volume and $\mathcal{H}$ the Heaviside step function. Equation (8) is evaluated on the fine G grid using an algebraic expression [51].

The third term impacted by the location of the interface is the surface force, represented by the term $\kappa\delta\hat{\mathbf{n}}/\mathrm{We}$ in Eq. (1), which in the staggered grid layout used here needs to be evaluated at the cell faces. Following the continuum surface force model [52], $\delta\mathbf{n}$ is approximated by $\delta\mathbf{n} = \nabla\alpha_{\mathrm{CV}}$. This results in the surface force calculated by

$$\frac{1}{\mathrm{We}}\kappa\delta\hat{\mathbf{n}} = \frac{1}{\mathrm{We}}\kappa\nabla\alpha_{\mathrm{CV}}, \tag{9}$$

with all terms being evaluated at the cell faces due to the staggered grid layout.

In this paper we are presenting a study of the basic state, which is steady and axisymmetric, and so we restrict our simulations to the axisymmetric Navier-Stokes equations. Nevertheless, this basic state is highly nontrivial with a deformed interface and thin boundary and interfacial shear layers. Numerical grid convergence studies are presented and discussed in the Appendix, which also contains the code verification test case of a two-phase solid-body rotation.

III. RESULTS

We present results for two classes of scenarios. In the first, we limit ourselves to physical systems that are easy to realize in order to provide comparison data for future experiments. In Sec. III A we analyze the effect of increasing the disk rotation rate and in Sec. III B we analyze the impact of viscosity ratio between the fluids by varying the silicone oil. In the second class, we analyze the impact of individual characteristic numbers on the system by varying only the Reynolds number in Sec. III C, only the Weber number in Sec. III D, and only the Froude number in Sec. III E. These analyzed systems can still be physically realized, however, they involve significantly more experimental effort.

A. Effects of increasing the disk rotation rate

We begin by examining the flow, starting from rest, for different rates of rotation of the bottom disk Ω. In nondimensional terms, this means considering various values of Re. Since Fr and We also depend on Ω, these will also vary. In this section, we consider all properties to correspond to a bottom fluid of Flourinert FC-75 and a top fluid of DOW-Corning DC-200 silicone oil with nominal viscosity 10 cS. The material property ratios are $\rho_r = 0.5284$ and $\mu_r = 6.9124$ and the surface tension between the two fluids is $\sigma = 7.0 \times 10^{-3}$ N/m [53]. Further, we shall set $H/R = 1.5$ and $h/R = 0.75$. To determine the parameters, we consider a cylinder of radius $R = 0.5$ cm on Earth (gravitational acceleration $g = 9.806\,65$ m/s^2).

Although the flow is computed using the velocity formulation as described in Sec. II, since the flows are axisymmetric, it is convenient to describe them in terms of the stream-function–vorticity formulation. The velocity field in the cylindrical polar coordinates (r,θ,z) is $\mathbf{u} = (u,v,w) = (-\psi_z/r,\gamma/r,\psi_r/r)$ and the corresponding vorticity field is $\nabla \times \mathbf{u} = (-\gamma_z/r,\eta,\gamma_r/r)$, where subscripts denote differentiation. Contours of ψ in a meridional plane (r,z) depict streamlines and contours of $\gamma = rv$ in that plane depict vortex lines. The azimuthal component of vorticity is related to the stream function by

$$\psi_{zz} + \psi_{rr} - \psi_r/r = -\eta/r. \tag{10}$$

The steady states for various Re (and corresponding Fr and We) are illustrated in Fig. 1, which shows the vortex lines (top panels), streamlines (middle panels), and contours of the azimuthal component of vorticity (bottom panels). The results for Re = 1200 and 1800 are qualitatively similar. Following the impulsive start of the bottom rotating disk, the disk boundary layer is rapidly established within about one disk rotation (by about $t = 6$). This is seen best in how the η contours adjacent to the disk reach a steady state in the associated online movie [54]. The fluid in this boundary layer is centrifuged radially outward, carrying the angular momentum acquired from the rotating disk with it (evidenced by the bending of the vortex lines radially outward in the layer), and a weak secondary meridional flow is established that replaces the centrifuged fluid with fluid from the interior. The streamlines illustrate this large-scale meridional circulation. As the centrifuged fluid is turned upward by the presence of the cylinder sidewall, a sidewall boundary layer is established on a slower time scale in which the angular momentum is advected upward. The sidewall layer is established by about $t = 35$. Since the flow has finite Re, there is some viscous diffusion of the advected angular momentum. As this sidewall boundary layer flow reaches the vicinity of the interface, there is some upward displacement of the interface, but for the most part, the fluid in the bottom layer is turned radially inward at the interface. Having a more viscous top layer of fluid, the inward radial velocity decreases as it gets closer to the interface, establishing a boundary layer that has much in common with that at a rigid no-slip wall; the structure of the η boundary layer at the interface is very similar to that at a no-slip wall in comparable parameter regimes (compare with results in Ref. [30]). Of course, the interface is not rigid or no slip and so there is nonzero flow tangential to the interface (the flow normal to the interface goes to zero as the flow asymptotically approaches a steady state, which is reached by about $t = 120$).

The velocity is continuous across the interface and the fluid in the top layer is dragged radially inward with the meridional flow in the bottom layer, thereby establishing a large-scale meridional flow in the top fluid. The top meridional flow is much weaker and has an opposite sense of circulation to that in the bottom layer. Of particular note, the radial velocity in both the top and bottom fluids near the interface is directed radially inward. The top layer of fluid is also spinning due to its contact with the interfacial layer that has acquired angular momentum. However, the top layer spins considerably less than the bottom layer in the vicinity of the interface as the vortex lines, while being continuous across the interface, are refracted and also undergo significant bending in the interfacial layer, where they are almost tangential to the interface over a good portion of it.

As Re is increased, the interface deforms more as the sidewall boundary-layer flow is stronger and can push the lower-denser fluid further up and to conserve mass the interface is lowered at the axis. Also, with increased Re, less of the angular momentum acquired in the rotating-disk boundary layer is dissipated as the fluid is advected faster to the interface and consequently the interfacial fluid is rotating faster with increased Re. The appropriate measure of how fast the interface is rotating is v/r along the interface. On the rotating disk, $v/r = 1$ for all Re. Figure 2(c) shows that v/r along the interface increases with Re and is largest at the axis and zero at the sidewall. At Re = 3000, for $r \lesssim 0.2$ the fluid in the bottom layer is close to solid-body rotation, as can be seen in Fig. 1 from the vortex lines (contours of rv), with weak meridional circulation (the streamlines are almost vertical and spaced widely apart, indicative of a slow effusive axial flow into the bottom disk boundary layer). The flow in the bottom

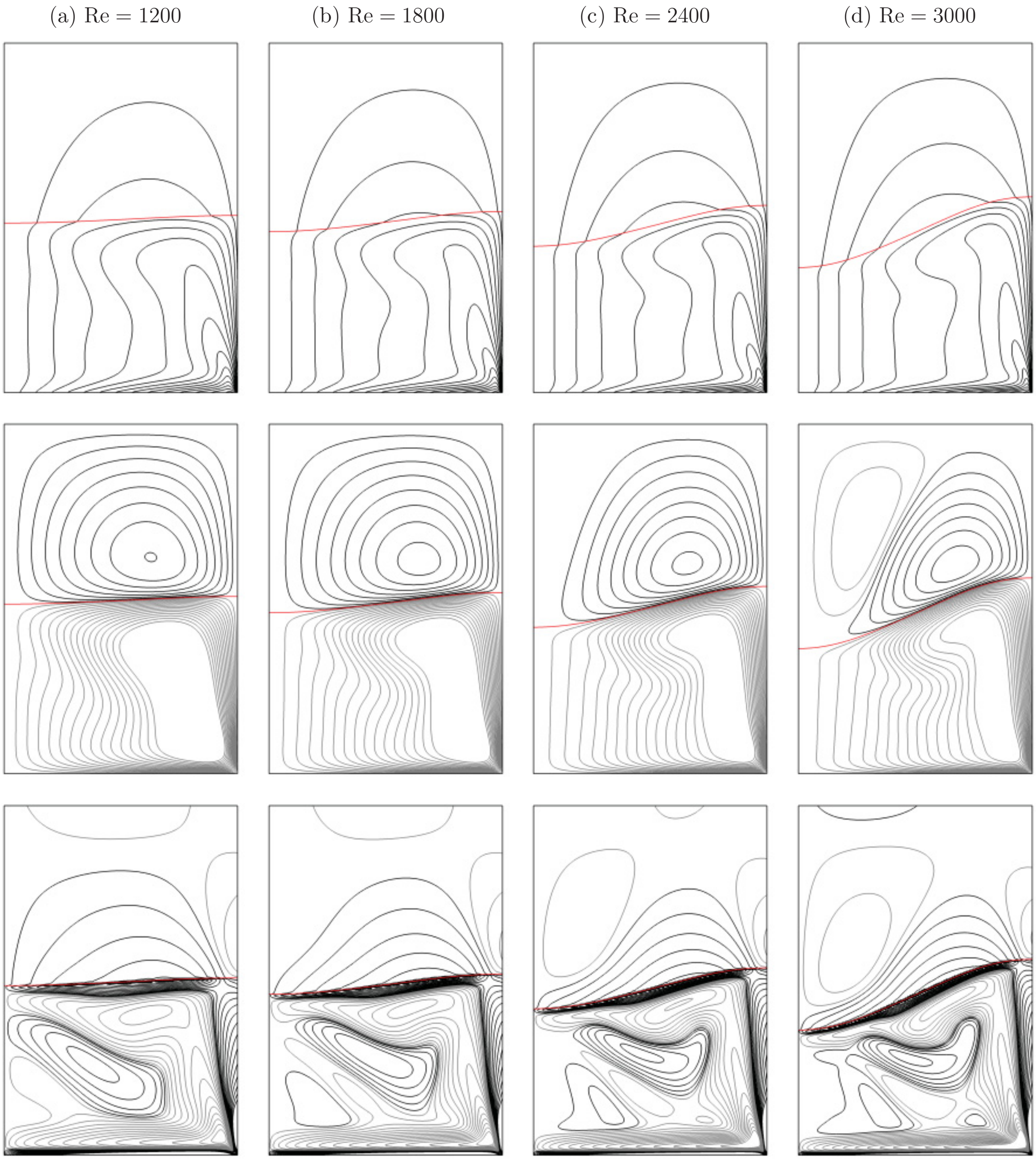

FIG. 1. (Color online) Contours at a steady state of vortex lines rv (top row), streamlines ψ (middle row), and azimuthal vorticity η (bottom row) at (a) Re = 1200, Fr = 0.887, and We = 41.0; (b) Re = 1800, Fr = 2.00, and We = 92.3; (c) Re = 2400, Fr = 3.55, and We = 164; and (d) Re = 3000, Fr = 5.55, and We = 256; these Fr and We numbers correspond to flow of Flourinert FC-75 (bottom fluid) and DOW-Corning DC-200 silicone oil (top fluid) in a cylinder of radius 0.5 cm on Earth. There are 15 positive (black) and 15 negative (gray) contour levels, given by $\mathcal{L}_i = \pm(i/15)^2$ max, where $\mathcal{L}$ denotes level and max = 0.005 for ψ and max = 3 for η. For rv, $\mathcal{L}_i = (i/15)^2$ as rv is non-negative and has a maximum value of 1 (see associated online movies [54]).

fluid for $r \gtrsim 0.2$ has a strong meridional circulation. This division into an inner-radius solid-body rotating flow and an outer-radius swirling flow with strong meridional circulation has been observed previously in experiments and simulations with both a stress-free interface and a surfactant-influenced interface [8,9,29]. The flow in the upper fluid is now influenced by the swirling interfacial flow. It is spun up in a fashion similar to that explored in Ref. [55] for the flow in a cylinder driven by a disk of smaller radius on the bottom end wall. The swirling interface for $r \lesssim 0.2$ now is able to centrifuge the upper fluid adjacent to it radially outward, thereby establishing a meridional circulation cell of opposite sense to the meridional circulation that is driven by the interface along $r \gtrsim 0.2$ [see the streamlines for Re = 3000 in Fig. 1(d)].

For all the Reynolds numbers considered, Re $\leqslant$ 3000, the interface displacement and curvature vary self-similarly with Re, as can be seen in Figs. 2(a) and 2(b). In fact, Fig. 3 shows that the curvature distribution collapses as $\kappa \mathrm{Re}^{-2.5}$. The interface rotation rate v/r also collapses self-similarly over the range of Re considered according to $\mathrm{Re}^{-0.75} v/r$. However,

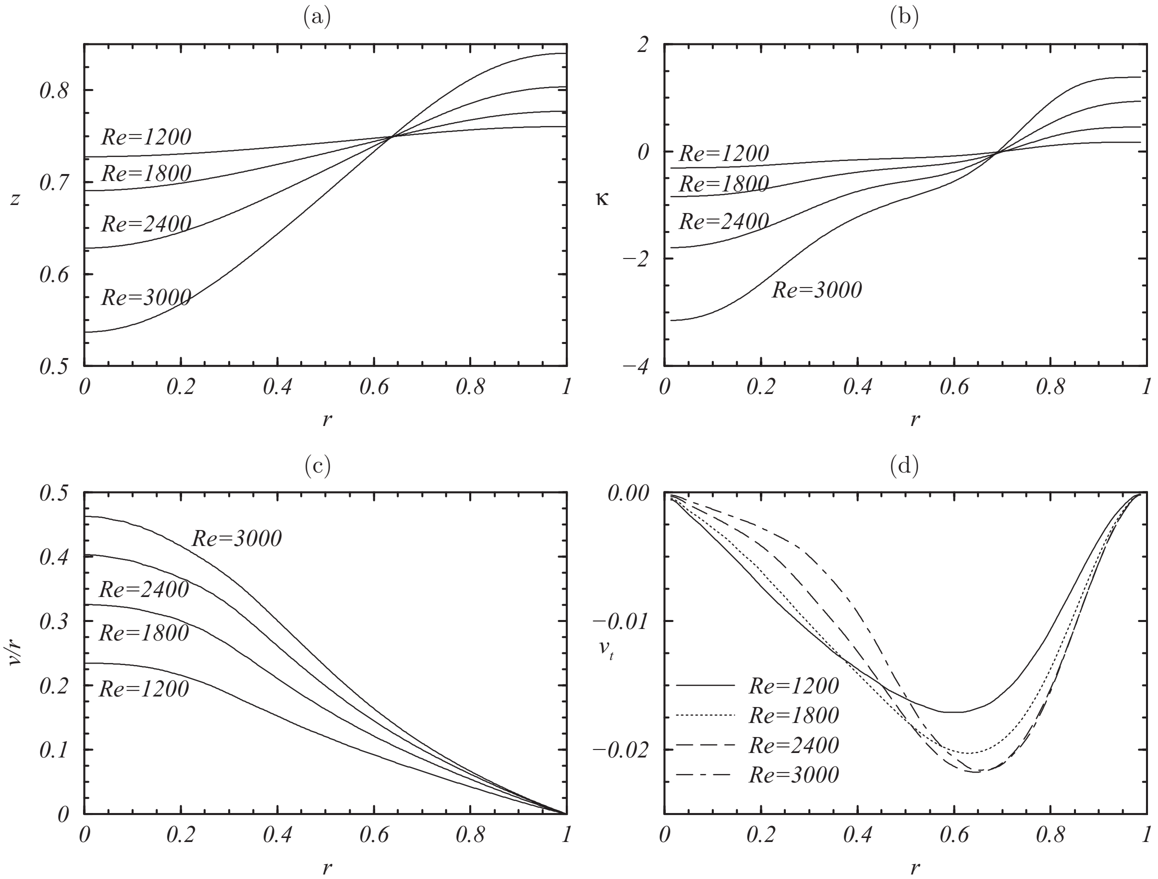

FIG. 2. Radial variations of the (a) interface height, (b) interface curvature, (c) rotation rate of the interface, and (d) meridional velocity tangential to the interface, for the corresponding steady-state solutions in Fig. 1.

the meridional velocity tangential to the interface v_t does not vary self-similarly with Re, as is evident from Fig. 2(d). The maximum negative v_t does not vary significantly with Re, remaining at about 2% of the maximum disk velocity, while in contrast v/r increases by 50% over the same range of Re. A maximum negative v_t also saturates at larger r as Re increases while v_t tends to zero over an increasing range of r out from the axis as Re increases. This is a consequence of the fluid in the top layer adjacent to the interface being centrifuged radially outward at the higher Re at small r as it rotates faster with increasing Re, leading to the counterrotating meridional flow near the axis and interface commented on earlier.

B. Effects of viscosity ratio μ_r

By utilizing a variety of silicone oils with different viscosities as the top layer, it is possible to keep all of the governing parameters other than μ_r essentially constant

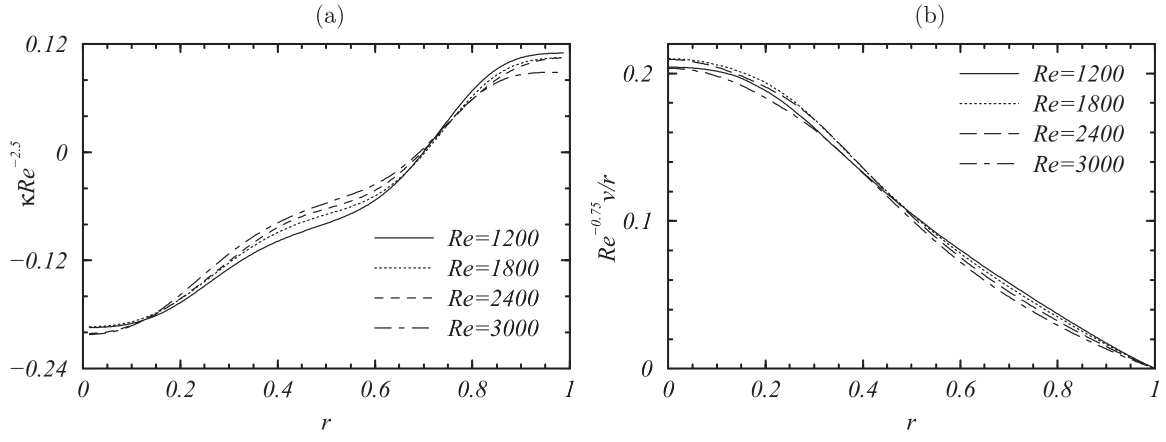

FIG. 3. Radial variations of the (a) interface curvature and (b) rotation rate of the interface for the corresponding steady-state solutions in Fig. 1.

in a physical experiment. In this section, we shall keep $\text{Re} = 2000$, $\text{Fr} = 2.46$, $\text{We} = 114$, $\rho_r = 0.5284$, $H/R = 1.5$, and $h/R = 0.75$ while varying μ_r from 100 down to 0.2 (for the silicone oil used in the preceding subsection, $\mu_r = 6.9124$, which we simply refer to as the $\mu_r = 7$ case for now). For comparison purposes, we also consider the flow where the interface between the top and bottom fluids is replaced by a rigid no-slip boundary and we solve for the flow in the bottom, with $\text{Re} = 2000$ and $H/R = 0.75$ (for this single-phase flow, Re and H/R are the only governing parameters).

The vortex lines rv, streamlines ψ, and azimuthal vorticity η for various μ_r are shown in Fig. 4, along with the no-slip interface case. Comparing the no-slip case with the flow in the bottom fluid of the $\mu_r = 100$ case [Figs. 4(a) and 4(b)], we find that the flows are essentially the same except for the nontrivial deformation of the interface. The deformation leads to a stretching of the vortex lines near the sidewall where the interface height is largest, resulting in a slightly faster azimuthal velocity there compared with the no-slip case, while the reduced interface height near the axis leads to the vortex lines being axially compressed and the solid-body rotation near the axis is slightly slower than in the no-slip case. The vortex lines are almost tangential to the interface, so that the top fluid, which is 100 times more viscous, is hardly spun up. Since the interface is not no slip, the meridional tangential velocity along the interface is also not zero and via the viscous coupling there is a weak meridional circulation in the top fluid as the top fluid adjacent to the interface is also dragged radially inward. In the limit of $\mu_r \to \infty$, it is expected that $v \to 0$ and $v_t \to 0$ on the interface, corresponding to the no-slip, rigid boundary condition. However, with everything else finite (in particular with finite Fr), there is still significant interface deformation at large μ_r.

For $\mu_r > 7$, the flows are qualitatively similar; the interface is slightly more deformed, the meridional tangential velocity is faster, and the meridional circulation in the top fluid is stronger for smaller μ_r. Of particular note, as μ_r is decreased, the vortex lines in the bottom fluid meet the interface at a larger angle, indicating that the interface is swirling faster with smaller μ_r, and this leads to an increasingly spun-up upper layer of fluid. On reducing μ_r to about 5, the interface is sufficiently spun up, especially near the axis, so as to centrifuge the fluid in the top layer adjacent to the interface radially outward, thus creating a meridional flow of the opposite sense in the

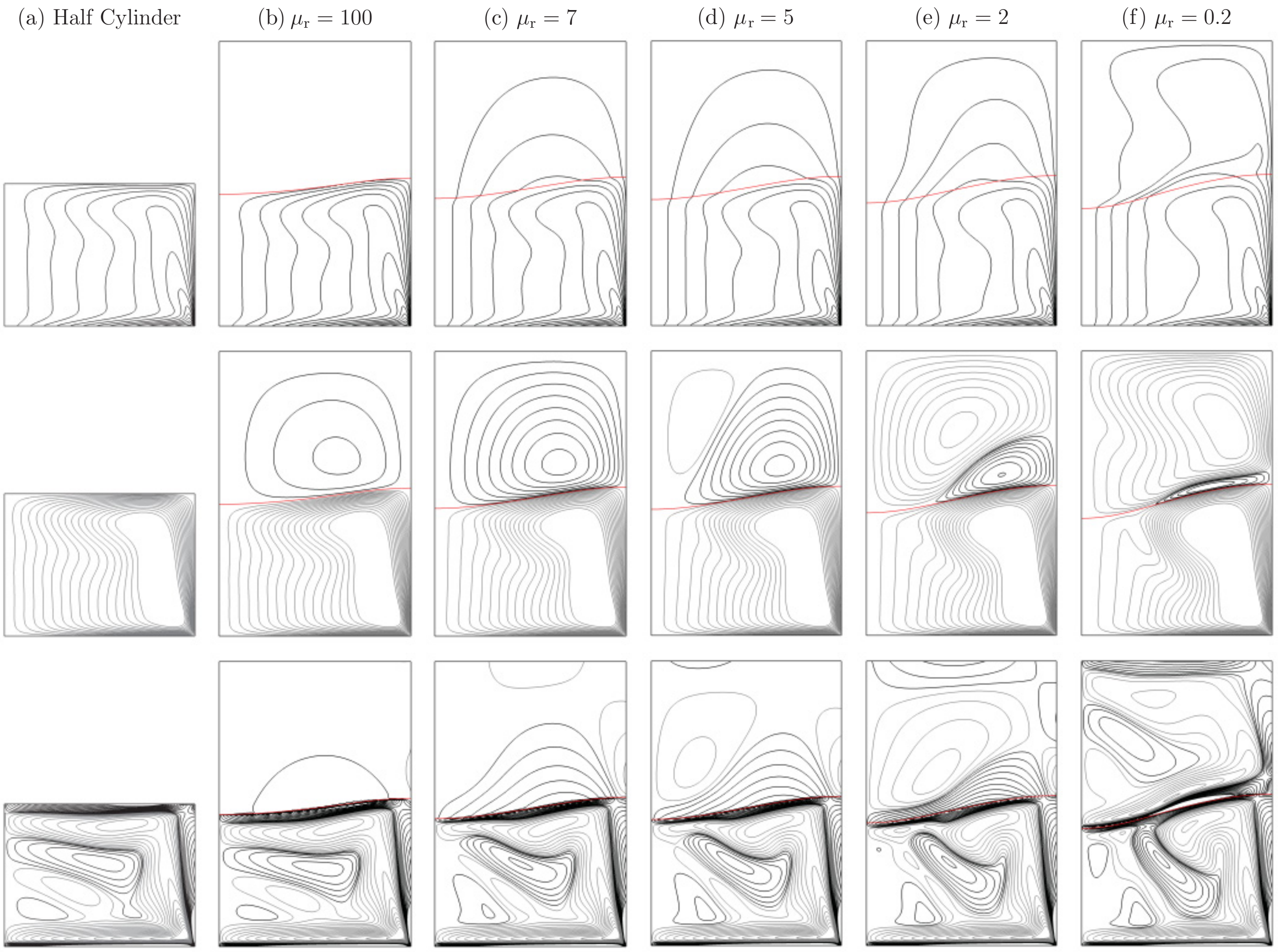

FIG. 4. (Color online) Contours at a steady state of vortex lines rv (top row), streamlines ψ (middle row), and azimuthal vorticity (bottom row) at $\text{Re} = 2000$, $\text{Fr} = 2.46$, $\text{We} = 114$, and viscosity ratios as indicated. The contour levels are the same as in Fig. 1 (see the associated online movies [54]).

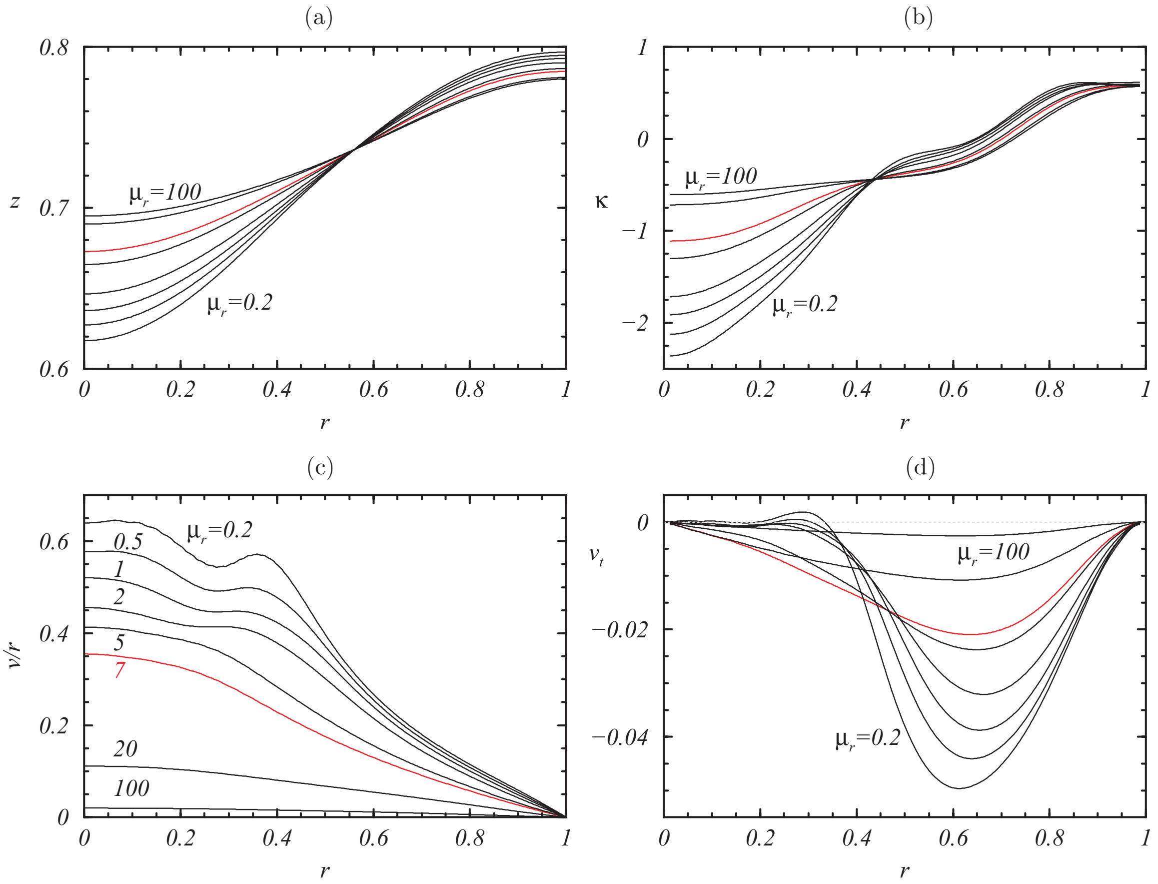

FIG. 5. (Color online) Radial variations of the (a) interface height, (b) interface curvature, (c) rotation rate of the interface, and (d) meridional velocity tangential to the interface, for the corresponding steady-state solutions in Fig. 4 at Re = 2000 and the indicated values of μ_r (the $\mu_r = 7$ case is shown in red).

upper fluid. As μ_r is further reduced, this counter meridional flow dominates in the upper fluid and the original meridional circulation that at larger μ_r was driven by the meridional circulation in the lower fluid is now confined to an increasingly thinner boundary-layer-type flow over the outer radial part of the interface at the smallest μ_r [see Fig. 4(f)]. At the smallest μ_r considered, the flow in the bottom fluid is most intense due to the reduced viscous damping from the upper fluid and the flow begins to resemble the swirling flows with a free upper surface, i.e., idealized flows with the upper fluid having zero viscosity and density and the interface having zero surface tension. In particular, Fig. 4(f) shows the development of a recirculation zone attached to the interface away from the axis, which is typical in free-surface swirling flow models as well as in experiments with air as the upper fluid and water as the lower fluid [2,3,5,15]. This recirculation zone tends to form near where the inner radial flow is in solid-body rotation and the outer radial flow is dominated by the meridional circulation [8,9].

The temporal evolutions from rest are affected by the viscosity ratio, as can be seen from the online movies [54] associated with Fig. 4. For large μ_r, the top fluid adjusts quickly to flow changes in the bottom fluid so that both reach a steady state essentially at the same time. In contrast, for small μ_r, the top fluid is slower to adjust to changes as the bottom fluid evolves, and then the delayed adjustments in the top fluid result in further adjustments in the bottom fluid, and so the transient flow is a damped oscillation.

Figures 5(a) and 5(b) show that in the outer radial region, the interface height and curvature are little affected by variations in μ_r. However, in the inner radial region, there are significant changes with the interface height dropping and the interface curvature becoming more negative as μ_r is decreased. This is attributable to the strengthening counter meridional flow and increased swirl in the upper fluid as μ_r is decreased. Notice from the contours of rv in Fig. 4 that the top fluid is spinning faster with decreasing μ_r, but that as μ_r is decreased below about 1, the stronger counter meridional flow in the top fluid advects the angular momentum to larger radii, leaving the inner radial region spinning slower as μ_r is decreased, while at the same time the interface is spinning faster [Fig. 5(c)]. It is this fast-spinning inner radial section of the interface that drives the counter meridional flow; its effect on the tangential meridional velocity at the interface v_t is shown in Fig. 5(d), where we find that v_t becomes positive (radial outflow) for $\mu_r < 1$ with $r < 0.35$ while there is an increasingly strong radial inflow (v_t negative) along the interface for $r > 0.35$ as μ_r is decreased.

C. Effects of varying Reynolds number

Up to now, we have considered parameter variations that are readily reproduced in laboratory experiments. However, these protocols vary the relative strengths of several forces, making it difficult to determine their individual contribution on the observed phenomena. In this section, we isolate the effect of inertia by varying only Re and keeping the other parameters fixed at We = 114, Fr = 2.46, $\mu_r = 6.9124$, $\rho_r = 0.5284$, $H/R = 1.5$, and $h/R = 0.75$ (corresponding to the two-fluid system considered in Sec. III A).

Figure 6 depicts radial variations in interface height, interface curvature, rotation rate, and meridional velocity tangential to the interface at a steady state for Re $\in [1200,3000]$. The degree by which the top fluid is spun up is similar to the case of varying Ω at the same Reynolds numbers. However, the interface at the same Re is significantly less deformed here.

As in the varying-rotation-rate case, the interface curvature and rotation rate of the interface collapse with a Reynolds number scaling (see Fig. 7). However, here, the best-fit exponents are -0.5 in both cases compared to -2.5 (curvature) and -0.75 (rotation rate) in the varying-Ω case. The reason for the change in fitting exponent, especially for the interface curvature, is the following. In the varying-Ω case, an increase in Ω results in an increase not only in Re, but also in We and Fr. The decrease in relative importance of surface tension (due to increasing We) leads to larger deformations of the interface and hence larger interfacial curvatures (see Figs. 2 and 6). This compares to the case here where only Re is varied and the relative importance of surface tension is kept constant. To collapse the larger curvature variations in the varying-Ω case thus required a higher power than in the constant-We-number case.

These results indicate that surface tension effects are of significance in the analyzed system, a point further analyzed in Sec. III D.

D. Effects of varying Weber number

In this section, we explore the effects of surface tension. Surface tension enters into the nondimensional system via the Weber number only. We set Re = 2000, Fr = 2.42, $\mu_r = 6.9124$, $\rho_r = 0.5284$, $H/R = 1.5$, and $h/R = 0.75$ (corresponding to the two-fluid system considered in Sec. III A) and consider four cases for different values of We: (a) We = 50, (b) We = 114 (corresponding to the Flourinert and silicone oil system), (c) We = 500, and (d) We = ∞ (zero surface tension). Physically, these variations in We may be obtained by choosing an appropriate silicone oil and heating the system

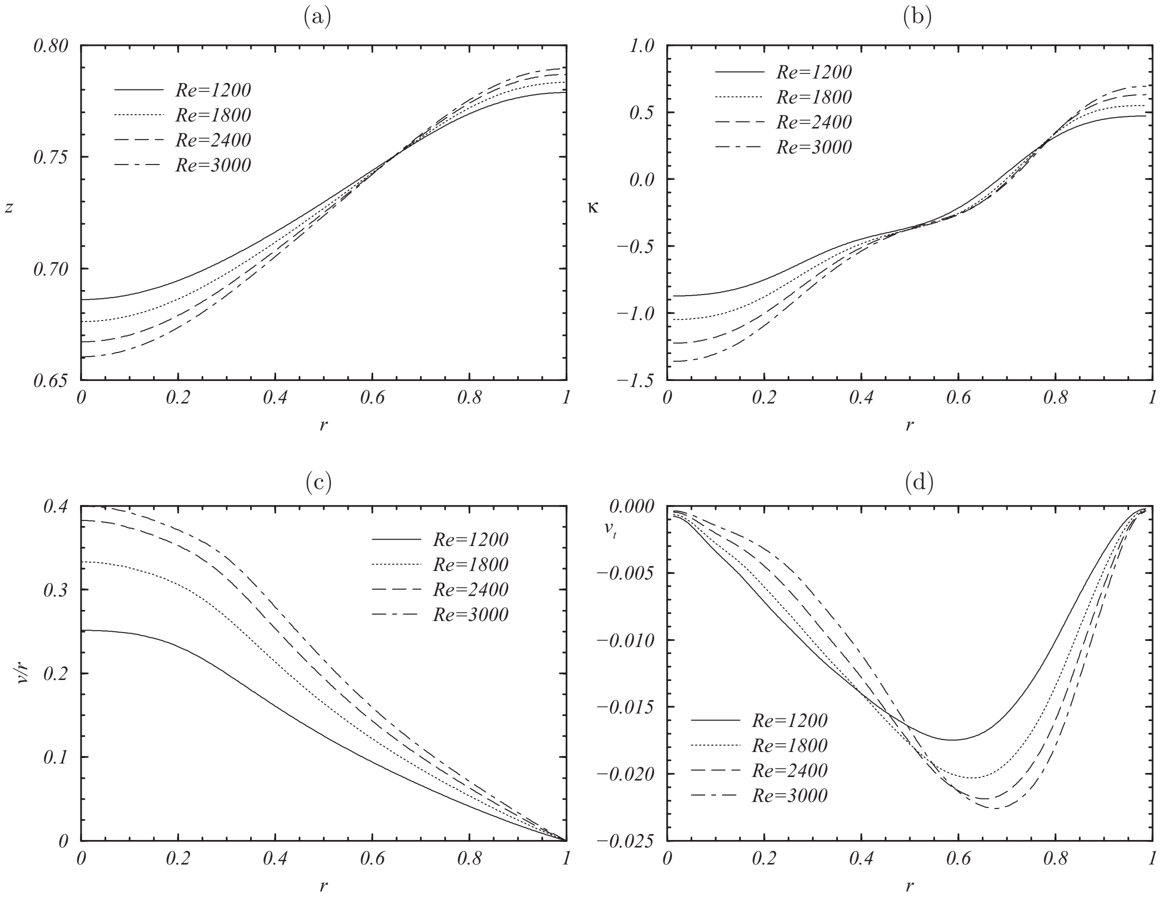

FIG. 6. Radial variations of the (a) interface height, (b) interface curvature, (c) rotation rate of the interface, and (d) meridional velocity tangential to the interface, for the steady-state solutions at Fr = 2.42, We = 114, and Re as indicated. These Fr and We numbers correspond to flow of Flourinert FC-75 (bottom fluid) and DOW-Corning DC-200 silicone oil (top fluid) in a cylinder with a radius of 0.5 cm on Earth at Re = 2000.

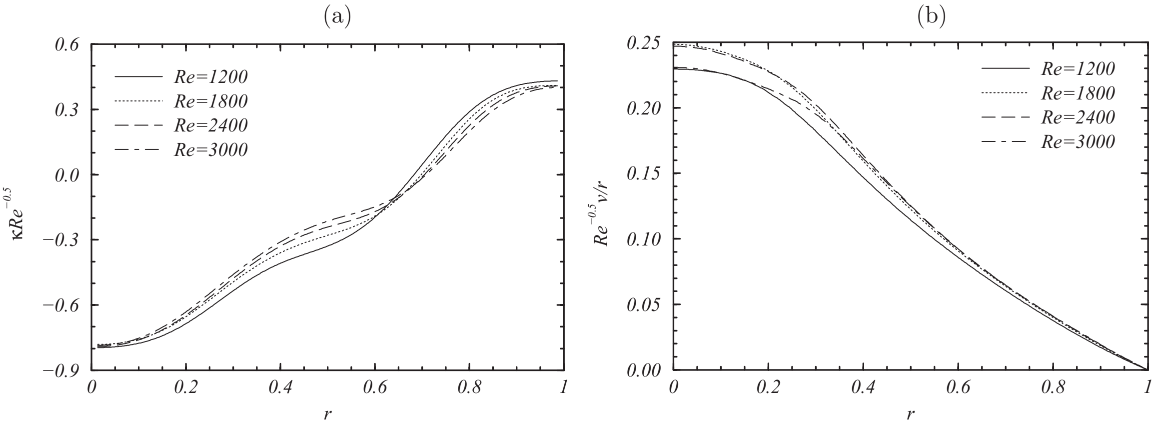

FIG. 7. Radial variations of the (a) interface curvature and (b) rotation rate of the interface for the same steady-state solutions as in Fig. 6.

to a uniform temperature such that the desired Re, Fr, and We are achieved.

Although meridional contour plots do not show much variation with Weber number, a close examination of the interfacial profiles show significant We dependences. These profiles are shown in Fig. 8 depicting radial variations in interface height, interface curvature, rotation rate, and meridional velocity tangential to the interface at a steady state for various We as indicated. In particular, the surface deformation increases as We increases and the curvature not only increases in magnitude but also shows large amplitude undulations reminiscent of a shear driven wave. In contrast, the interface rotation rate and meridional velocity tangential to the interface are quite insensitive to Weber-number variations.

Surface tension effects are important in determining the steady-state shape of the interface in these flows. The question

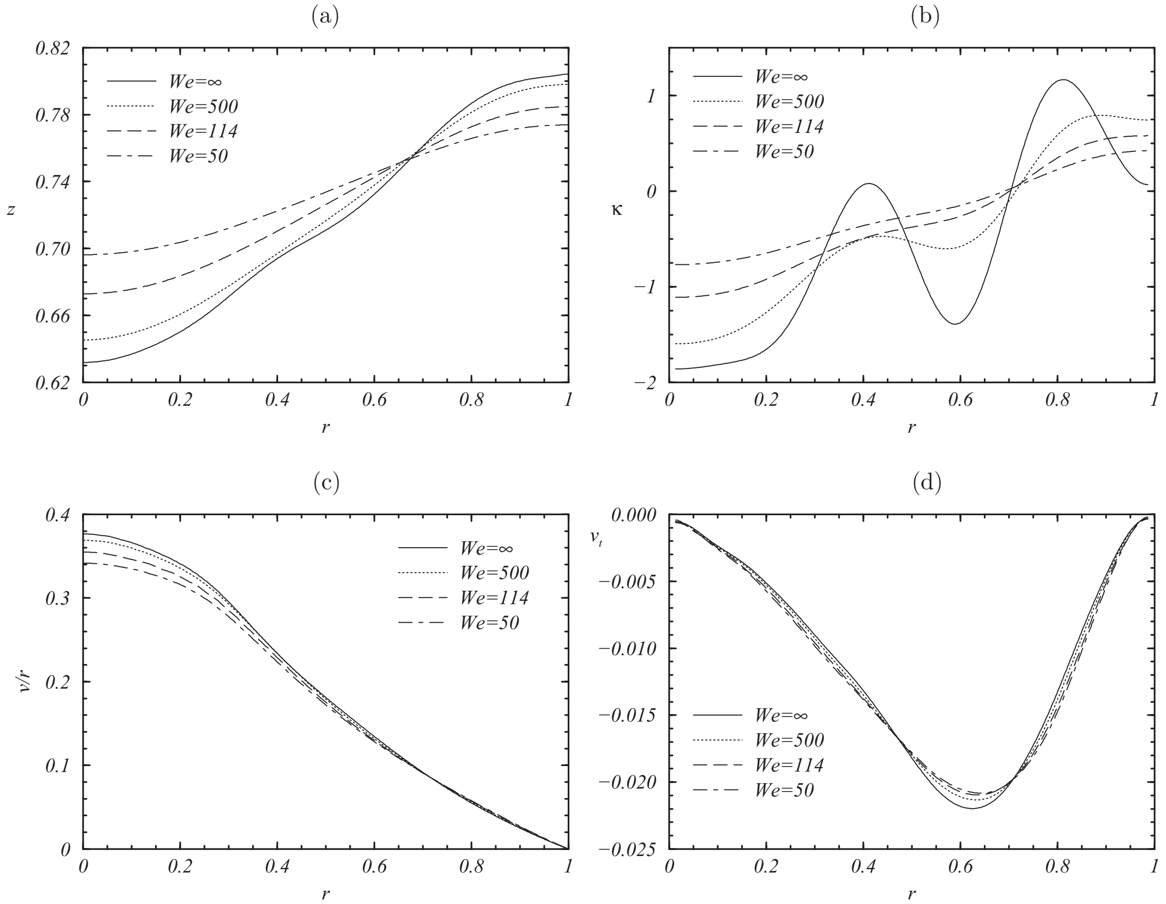

FIG. 8. Radial variations of the (a) interface height, (b) interface curvature, (c) rotation rate of the interface, and (d) meridional velocity tangential to the interface, for the steady-state solutions at Fr = 2.42, Re = 2000, and We as indicated. These Fr and Re numbers correspond to flow of Flourinert FC-75 (bottom fluid) and DOW-Corning DC-200 silicone oil (top fluid) in a cylinder with a radius of 0.5 cm on Earth.

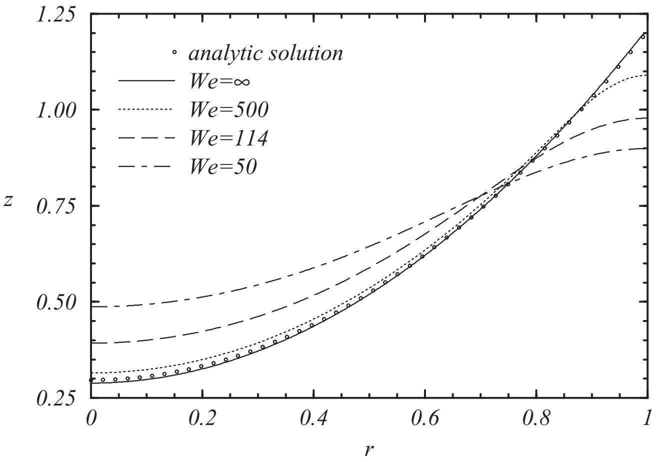

FIG. 9. Profiles of interface height for the case of two-phase solid-body rotation for the case with zero surface tension, physical surface tension, and analytical solution. The analytical solution is $z = h/R[1 + \mathrm{Fr}(2r^2 - 1)/4]$, with $h/R = 0.75$ and $\mathrm{Fr} = 2.42$.

then is whether this is due to the peculiarities of the chosen flow configuration with high shear. To analyze this, Fig. 9 shows the two-phase solid-body rotation test case used in the Appendix to verify the code, but now with the addition of surface tension. As clearly shown, an increase in surface tension (lower We) results in significantly different interface shapes, flattening the interface. This raises a concern of trying to reproduce these results experimentally using so-called essentially immiscible fluids, i.e., fluids that are miscible on a much slower time scale than the time scale on which experiments are conducted, since such systems lack surface tension.

E. Effects of varying Froude number

In this section, we explore the effects of gravity, which only enters into the nondimensional system via the Froude number. Physically, one could explore such Froude number variation effects by conducting the same experiment in a low-gravity environment. Numerically, we set $\mathrm{Re} = 2000$, $\mathrm{We} = 114$, $\rho_r = 0.5284$, $\mu_r = 6.9124$, $H/R = 1.5$, and $h/R = 0.75$ (corresponding to the Flourinert and silicone oil system considered in Sec. III A) and consider three Fr cases: (i) $\mathrm{Fr} = 6.3 \times 10^{-5}$, corresponding to a very large gravity so that the interface is essentially flat; (ii) $\mathrm{Fr} = 2.46$, corresponding to the Earth's gravity; and (iii) $\mathrm{Fr} = \infty$, corresponding to zero gravity.

There are very few consequences beyond interfacial curvature to having a change in gravity. The $\mathrm{Fr} \approx 0$ case has the least deformation, with the interface being essentially flat, and the $\mathrm{Fr} = \infty$ case has the maximum deformation. The amount of deformation, even at $\mathrm{Fr} = \infty$, is limited by surface tension effects ($\mathrm{We} = 114$), as is evident in Figs. 10(a) and 10(b), which show the interface shape and curvature,

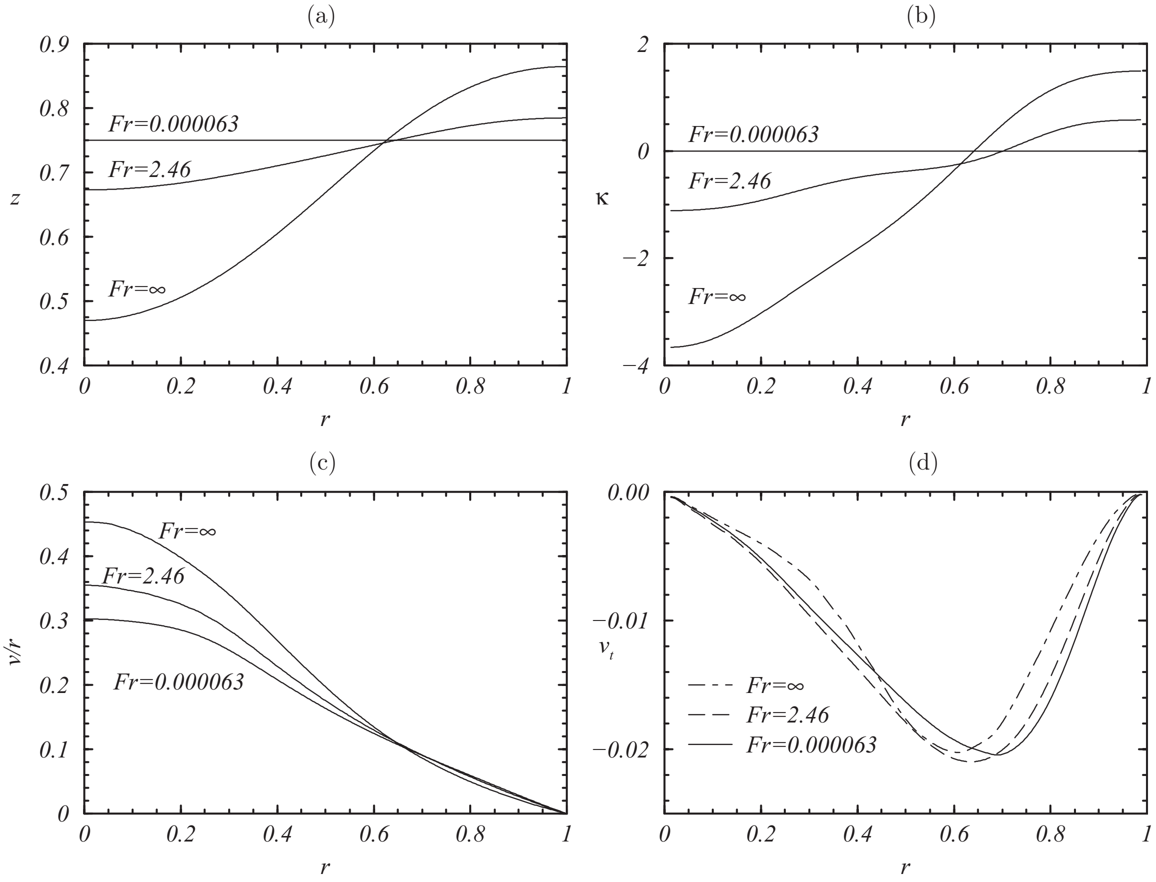

FIG. 10. Radial variations of the (a) interface height, (b) interface curvature, (c) rotation rate of the interface, and (d) meridional velocity tangential to the interface, for the steady-state solutions at $\mathrm{Re} = 2000$, $\mathrm{We} = 114$, and Fr as indicated.

respectively. The flows not very close to the interface are very similar, especially in the upper fluid. Near the interface the flows simply adjust to the change in shape of the interface. However, more careful inspection near the interface does reveal some curvature effects. In particular, the way in which the vortex lines rv meet and cross the interface is affected by the curvature and this results in the interface rotation v/r varying with Fr. Figure 10(c) shows that the interface rotation increases by about 50% from the flat interface case to the most deformed interface case. This increase in interface rotation is in the inner radial section where the bulk flow in the bottom fluid is nearly in solid-body rotation. However, the meridional tangential velocity v_t is affected very little by the interface deformation [Fig. 10(d)]. This all indicates that the interface deformation primarily affects how the vortex lines meet and bend at the interface and any effects on the meridional flows are primarily a consequence of the vortex line bending.

Comparing the flat interface case ($\mathrm{Fr} \approx 0$) with the rigid lid case, we find that the flow in the lower fluid is very similar. The main distinction is that the η-boundary layer in the rigid lid case has approximately uniform thickness, whereas that in the small-Fr case is considerably thinner for $r < 0.25$. This is attributable to the difference in the behavior of the vortex lines in this region. With the rigid lid case, the vortex lines are bent in the boundary layer to be tangential to the stationary lid, whereas for the small-Fr case, the vortex lines are not bent very much. Where the bulk lower fluid is in near solid-body rotation, the vortex lines cross the interface and the interface spins. Where the bottom fluid is primarily overturning meridionally, the vortex lines are almost tangential to the interface and its rotation is greatly reduced. The vortex line bending is a local source of azimuthal vorticity [3,56] and is responsible for the establishment of the interfacial shear layer.

IV. CONCLUSION

We have studied numerically the swirling flows of two immiscible fluids within a stationary enclosed cylinder driven by the uniform rotation of the bottom end wall. Initially, everything is at rest with the denser fluid in a bottom layer of equal volume to that of the lighter top fluid. Since only the bottom fluid is in contact with the rotating end wall, the top fluid is only driven into motion via the viscous coupling between the two fluids. The interface is deformable and its motion is determined by the balance between flow inertia, viscous stresses, gravitational buoyancy, and surface tension. We have considered a wide range of viscosity ratios of the two fluids μ_r and found that this plays an important role in determining the dynamics in the two fluids. When the top fluid is significantly more viscous than the bottom fluid, the top fluid adjusts quickly to the bottom flow, whereas for top fluids with smaller viscosity, the top fluid adjusts more slowly and this delay is fed back to the lower fluid, which then needs to readjust, leading to oscillatory transients. The viscous coupling between the two fluids is accomplished via the establishment of an interfacial shear layer due to the difference in the rotations of the top and bottom fluids.

As noted from theoretical analysis [40] and experiments [36] for the spin up of two essentially immiscible fluids, the interfacial shear layer is dynamically important. We also find this to be the case in the present problem. Much of the structure of the interfacial shear layer results from vortex line bending in the interfacial region and the amount of vortex line bending is strongly influenced by the viscosity ratio. Two extremes are typically well studied: $\mu_r \to \infty$, where the top fluid then acts like a no-slip boundary for the lower fluid and the vortex lines are bent to be tangential to the boundary, and $\mu_r \to 0$, which corresponds to a vacuum above the lower fluid and the vortex lines are normal to the interface in the lower fluid (this often provides a good model when the upper fluid is a gas). In this study, we have considered finite $\mu_r \in [0.2, 100]$, over which the amount of vortex line bending in the neighborhood of the interface varies considerably. As observed in Ref. [36], if the dynamics of the interfacial shear layer is not included, as in the theory of Ref. [39], then the lack of surface stresses leads to vortex stretching being the primary mechanism by which the interface moves. In our problem, vortex stretching effects are negligible compared with vortex bending effects.

Vortex stretching occurs when the vortex lines are stretched due to changes in the fluid depth, i.e., via interface deformation, which would correspond to increased or decreased axial vorticity, i.e., the vortex lines would be closer together or further apart. However, this is not evident from the results with $\mathrm{Fr} = 0$ and large Fr, which affect only the degree of interface deformation, and in and of itself does not contribute to the development of the interfacial layer, which is characterized by large concentrated azimuthal vorticity. In contrast, vortex line bending is clearly observed over all parameter ranges and the bending of vortex lines is a direct source of azimuthal vorticity. The vortex line bending is predominant in the interfacial layer as well as in the end-wall boundary layers. Another source of azimuthal vorticity at the interface is due to the surface tension term, but this is a small contribution compared to the vortex line bending. This is born out by the comparison between the $\mathrm{Fr} = 0$ case (where there is no surface tension term contribution to the azimuthal vorticity) and the large-Fr cases (leading to large deformations). The intensity of the interfacial layer's azimuthal vorticity is comparable for all Fr and hence primarily due to vortex line bending.

Pedlosky [40] included the interfacial shear layer due to finite μ_r, but took the limit of $\mathrm{Fr} \to 0$ so that the interface remained flat during the spin-up process and so his theory did not include surface tension effects (due to zero interfacial curvature). He concluded that the frictional coupling between the two fluids is vital for the spin-up process, which we find to be true here as well, but interfacial deformations and surface tension effects limiting the deformations are also critically important in the regimes we have studied.

TABLE I. Grid convergence for kinetic energy at $\mathrm{Re} = 3000$.

n_z	E_k	Error	Order
150	5.66×10^{-2}	1.00×10^{-3}	
300	5.58×10^{-2}	2.38×10^{-4}	2.07
450	5.57×10^{-2}	5.55×10^{-5}	3.59
600	5.56×10^{-2}		

TABLE II. Grid convergence for interface displacement Δh at $\mathrm{Re} = 3000$.

n_z	Δh	Error	Order
150	3.104×10^{-1}	8.106×10^{-3}	
300	3.030×10^{-1}	6.960×10^{-4}	3.54
450	3.025×10^{-1}	2.260×10^{-4}	2.77
600	3.023×10^{-1}		

ACKNOWLEDGMENTS

This work was supported by the US National Science Foundation Grants No. DMS-0808045 and No. DMS-0922864 and Korea Science and Engineering Foundation WCU Grant No. R32-2009-000-20021-0. Computations were performed using the ASU Advanced Computing Center (A2C2) and the NSF Teragrid Ranger cluster (TG-DMS090031).

APPENDIX: NUMERICAL RESOLUTION TESTS

To determine the appropriate numerical resolution, a grid convergence study was conducted for $\mathrm{Re} = 3000$ with the four resolutions: $(n_r, n_z) = (100,150)$, $(200,300)$, $(300,450)$, and $(400,600)$. Having the thinnest viscous boundary layer, the $\mathrm{Re} = 3000$ case requires the highest resolution of the cases considered in this paper. As such, any grid that is in the asymptotic convergence regime for the $\mathrm{Re} = 3000$ case will also be in that regime for the other parameters studied in this paper.

The largest difference between f_{600} and f_{150} occurs in the viscous boundary layer at the rotating bottom wall, suggesting that the coarsest grid (100×150) does not provide adequate resolution in this region. However, as the resolution is increased, the error rapidly decreases. The kinetic energy $E_k = \pi \int_0^{H/R} \int_0^1 (u^2 + v^2 + w^2) r \, dr \, dz$ is a useful global metric to determine convergence. Table I shows the kinetic energy for the indicated grid resolution. The error and order of convergence are computed using the results from the finest grid as the exact solution. The errors decrease with increasing grid resolution. The obtained order of convergence is slightly better than expected. This is most likely because kinetic energy is not directly simulated but is rather the sum of the squares of simulated variables, which leads to fortuitous cancellation of errors.

The interface position can also be used to determine the asymptotic convergence regime. The interface profiles of the finest grids lie directly on top of each other, while that of the coarsest grid is different from the others, demonstrating that the coarsest grid may not be in the asymptotic convergence regime. Table II shows the overall interface displacement for the indicated grid resolutions. The error and order of convergence are computed using the results from the finest grid as the exact solution.

To demonstrate grid convergence using local quantities, the velocity field at two points near the bottom right corner is examined. The points chosen are $(r,z) = (0.99,0.01)$, which is inside the viscous sublayer, and $(r,z) =$

TABLE III. Grid convergence for velocity fields at $(r,z) = (0.99,0.01)$.

n_z	u	Error	Order
150	2.071×10^{-2}	5.117×10^{-3}	
300	1.667×10^{-2}	1.083×10^{-3}	2.24
450	1.588×10^{-2}	2.850×10^{-4}	3.29
600	1.559×10^{-2}		
n_z	v	Error	Order
150	3.422×10^{-1}	-2.055×10^{-1}	
300	4.751×10^{-1}	-7.261×10^{-2}	1.50
450	5.231×10^{-1}	-2.463×10^{-2}	2.66
600	5.477×10^{-1}		
n_z	w	Error	Order
150	1.606×10^{-2}	5.641×10^{-4}	
300	1.585×10^{-2}	3.555×10^{-4}	0.67
450	1.561×10^{-2}	1.130×10^{-4}	2.83
600	1.549×10^{-2}		

TABLE IV. Grid convergence for velocity fields at $(r,z) = (0.98,0.02)$.

n_z	u	Error	Order
150	4.761×10^{-2}	1.451×10^{-3}	
300	4.646×10^{-2}	2.991×10^{-4}	2.28
450	4.622×10^{-2}	5.956×10^{-5}	3.98
600	4.616×10^{-2}		
n_z	v	Error	Order
150	6.064×10^{-1}	-6.122×10^{-2}	
300	6.478×10^{-1}	-1.982×10^{-2}	1.63
450	6.611×10^{-1}	-6.568×10^{-3}	2.72
600	6.676×10^{-1}		
n_z	w	Error	Order
150	4.920×10^{-2}	6.287×10^{-3}	
300	4.448×10^{-2}	1.573×10^{-3}	2.00
450	4.337×10^{-2}	4.665×10^{-4}	3.00
600	4.291×10^{-2}		

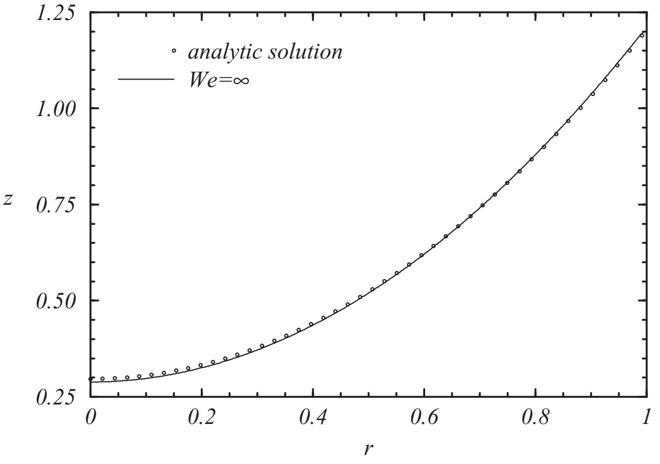

FIG. 11. Profiles of interface height for the case of two-phase solid-body rotation with zero surface tension. The analytical solution is $z = h/R[1 + \mathrm{Fr}(2r^2 - 1)/4]$, with $h/R = 0.75$ and $\mathrm{Fr} = 2.42$.

(0.98,0.02). The convergence test results, summarized in Tables III and IV, demonstrate that a numerical resolution of $n_r \times n_z = 200 \times 300$ is sufficient to ensure that the solution is within the asymptotic convergence regime. This is the grid resolution employed for results presented in this paper.

Having established that a grid converged solution can be reached, next we address the question whether convergence to the correct solution is achieved. To verify this, we compare our numerical results to an analytical solution in the case of solid-body rotation of two immiscible fluids. Figure 11 shows the radial profiles of the analytic interface (open symbols) and our computed profile (solid line). The analytical solution is derived assuming zero surface tension. The agreement between the analytical and numerical solutions is excellent, thus providing additional verification of the numerical code.

[1] G. H. Vatistas, J. Fluid Mech. **217**, 241 (1990).
[2] A. Spohn, M. Mory, and E. J. Hopfinger, Expt. Fluids **14**, 70 (1993).
[3] J. M. Lopez, Phys. Fluids **7**, 2700 (1995).
[4] A. Spohn, M. Mory, and E. J. Hopfinger, J. Fluid Mech. **370**, 73 (1998).
[5] M. Brons, L. K. Voigt, and J. N. Sorensen, J. Fluid Mech. **428**, 133 (2001).
[6] A. H. Hirsa, J. M. Lopez, and R. Miraghaie, Phys. Fluids **14**, L29 (2002).
[7] R. Miraghaie, J. M. Lopez, and A. H. Hirsa, Phys. Fluids **15**, L45 (2003).
[8] J. M. Lopez, F. Marques, A. H. Hirsa, and R. Miraghaie, J. Fluid Mech. **502**, 99 (2004).
[9] J. M. Lopez and F. Marques, J. Fluid Mech. **507**, 265 (2004).
[10] R. Iwatsu, J. Phys. Soc. Jpn. **74**, 333 (2005).
[11] T. R. N. Jansson, M. P. Haspang, K. H. Jensen, P. Hersen, and T. Bohr, Phys. Rev. Lett. **96**, 174502 (2006).
[12] T. Suzuki, M. Iima, and Y. Hayase, Phys. Fluids **18**, 101701 (2006).
[13] E. Serre and P. Bontoux, Int. J. Heat Fluid Flow **28**, 229 (2007).
[14] G. H. Vatistas, H. A. Abderrahmane, and M. H.Kamran Siddiqui, Phys. Rev. Lett. **100**, 174503 (2008).
[15] D. Lo Jacono, M. Nazarinia, and M. Brons, Phys. Fluids **21**, 111704 (2009).
[16] R. Bouffanais and D. Lo Jacono, Computers and Fluids **38**, 1651 (2009).
[17] R. Bouffanais and D. Lo Jacono, Phys. Fluids **21**, 064107 (2009).
[18] Y. Tasaka and M. Iima, J. Fluid Mech. **636**, 475 (2009).
[19] H. A. Abderrahamne, K. Siddiqui, and G. H. Vatistas, Phys. Rev. E **80**, 066305 (2009).
[20] S. J. Cogan, K. Ryan, and G. J. Sheard, J. Fluid Mech. **672**, 521 (2011).
[21] Y. Tasaka, K. Ito, and M. Iima, J. Visualization **11**, 163 (2008).
[22] J. M. Lopez and J. Chen, J. Fluids Eng. **120**, 655 (1998).
[23] J. M. Lopez and A. Hirsa, J. Colloid Interface Sci. **206**, 231 (1998).
[24] J. M. Lopez and A. Hirsa, J. Colloid Interface Sci. **229**, 575 (2000).
[25] A. H. Hirsa, J. M. Lopez, and R. Miraghaie, J. Fluid Mech. **443**, 271 (2001).
[26] A. H. Hirsa, J. M. Lopez, and R. Miraghaie, J. Fluid Mech. **470**, 135 (2002).
[27] M. J. Vogel, R. Miraghaie, J. M. Lopez, and A. H. Hirsa, Langmuir **20**, 5651 (2004).
[28] A. N. Azadani, J. M. Lopez, and A. H. Hirsa, Langmuir **23**, 5227 (2007).
[29] A. N. Azadani, J. M. Lopez, and A. H. Hirsa, J. Colloid Interface Sci. **322**, 79 (2008).
[30] J. M. Lopez, J. Fluid Mech. **221**, 533 (1990).
[31] J. C. R. Hunt, D. D. Stretch, and S. E. Belcher, J. Fluid Mech. **671**, 96 (2011).
[32] Y. Hasegawa and N. Kasagi, Int. J. Heat Mass Transfer **52**, 1012 (2009).
[33] J. E. Hart, Geophys. Astrophys. Fluid Dyn. **3**, 181 (1972).
[34] R. W. Griffiths and P. F. Linden, J. Fluid Mech. **105**, 283 (1981).
[35] J. E. Hart and S. Kittelman, Geophys. Astrophys. Fluid Dyn. **36**, 179 (1986).
[36] J. O'Donnell and P. F. Linden, Geophys. Astrophys. Fluid Dyn. **66**, 47 (1992).
[37] P. F. Linden and G. F. F. van Heijst, J. Fluid Mech. **143**, 69 (1984).
[38] A. M. Hogg and R. W. Griffiths, Ocean Modelling **35**, 54 (2010).
[39] J. R. Holton, J. Atmos. Sci. **22**, 402 (1965).
[40] J. Pedlosky, J. Fluid Mech. **28**, 463 (1967).
[41] A. S. Berman, J. Bradford, and T. S. Lundgren, J. Fluid Mech. **84**, 411 (1978).
[42] G. R. Baker and M. Israeli, Stud. Appl. Math. **65**, 249 (1981).
[43] G. R. Baker and S. J. Mardeusz, Stud. Appl. Math. **67**, 63 (1982).
[44] K. Y. Kim and J. M. Hyun, J. Fluids Eng. **116**, 808 (1994).
[45] S. Fujimoto and Y. Takeda, Phys. Rev. E **80**, 015304 (2009).
[46] S. Fujimoto, Y. Murai, Y. Tasaka, and Y. Takeda, J. Visualization **13**, 17 (2010).
[47] M. Herrmann, J. Comput. Phys. **227**, 2674 (2008).
[48] G.-S. Jiang and D. Peng, SIAM J. Sci. Comput. **21**, 2126 (2000).
[49] C. W. Shu, SIAM J. Sci. Stat. Comput. **9**, 1073 (1988).
[50] O. Desjardins, G. Blanquart, G. Balarac, and H. Pitsch, J. Comput. Phys. **227**, 7125 (2008).
[51] S. P. van der Pijl, A. Segal, and C. Vuik, Int. J. Numer. Meth. Fluids **47**, 339 (2005).
[52] J. U. Brackbill, D. B. Kothe, and C. Zemach, J. Comput. Phys. **100**, 335 (1992).
[53] P. H. Hadland, R. Balasubramaniam, G. Wozniak, and R. S. Subramanian, Expt. Fluids **26**, 240 (1999).
[54] See Supplemental Material at http://link.aps.org/supplemental/10.1103/PhysRevE.85.016308 for associated movies showing temporal evolutions of the flows starting from rest.
[55] M. Piva and E. Meiburg, Phys. Fluids **17**, 063603 (2005).
[56] P. A. Davidson, J. Fluid Mech. **209**, 35 (1989).